ACS APPLIED MATERIALS & INTERFACES

Research Article

www.acsami.org

Carbon-Coated Fe–Mn–O Composites as Promising Anode Materials for Lithium-Ion Batteries

Tao Li,[†] Yue-Ya Wang,[†] Rui Tang,[†] Yong-Xin Qi,[†] Ning Lun,[†] Yu-Jun Bai,*[,†,‡] and Run-Hua Fan*[,†]

[†]Key Laboratory for Liquid–Solid Structural Evolution and Processing of Materials (Ministry of Education), Shandong University, Jinan 250061, People's Republic of China

[‡]State Key Laboratory of Crystal Materials, Shandong University, Jinan 250100, People's Republic of China

Supporting Information

ABSTRACT: Fe–Mn–O composite oxides with various Fe/Mn molar ratios were prepared by a simple coprecipitation method followed by calcining at 600 °C, and carbon-coated oxides were obtained by pyrolyzing pyrrole at 550 °C. The cycling and rate performance of the oxides as anode materials are greatly associated with the Fe/Mn molar ratio. The carbon-coated oxides with a molar ratio of 2:1 exhibit a stable reversible capacity of 651.8 mA h g^{-1} at a current density of 100 mA g^{-1} after 90 cycles, and the capacities of 567.7, 501.3, 390.7, and 203.8 mA h g^{-1} at varied densities of 200, 400, 800, and 1600 mA g^{-1}, respectively. The electrochemical performance is superior to that of single Fe_3O_4 or MnO prepared under the same conditions. The enhanced performance could be ascribed to the smaller particle size of Fe–Mn–O than the individuals, the mutual segregation of heterogeneous oxides of Fe_3O_4 and MnO during delithiation, and heterogeneous elements of Fe and Mn during lithiation.

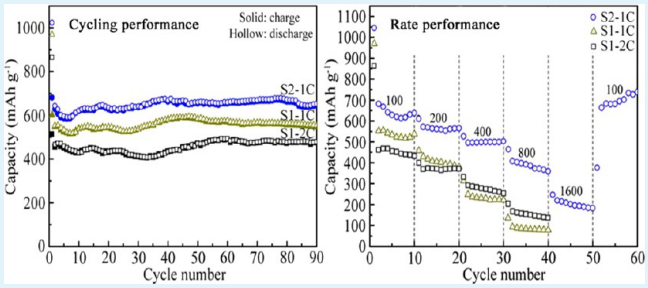

KEYWORDS: *cycling performance, rate capability, composite oxide, coprecipitation, electrochemical performance, anode material*

1. INTRODUCTION

Rechargeable lithium-ion batteries (LIBs) are currently being explored for high-power energy applications in electric vehicles, portable electronic devices and etc. Though graphite is the most commonly used anode material in LIBs, the low theoretical capacity of 372 mAh g^{-1} restricts the application in large-scale energy storage devices. Thus, intensive research has been focused on searching for other alternative anode materials to substitute for graphite. Transition-metal oxides (TMOs) have been paid more and more attention these years,[1−7] because their high theoretical capacity of more than 700 mAh g^{-1} might meet the ever-increasing energy demand. However, the practical applications of the TMOs are hindered by fast capacity fading, poor cycling performance and rate capability resulting from severe aggregation, low electronic conductivity, and large volume change during lithiation/delithiation. So far, several measures, such as refining the particles to nanoscale,[1,8,9] coating carbon on the nanoparticles,[10−12] compositing with other materials,[13−16] forming hollow or porous structures,[2,17−20] and doping with heterogeneous elements,[21,22] have been taken to mitigate the aggregation and large volume variation and to increase the electronic conductivity.

Among the TMOs, iron oxides and manganese oxides have some marked advantages over the others due to their low cost, eco-friendliness, natural abundance, and high energy density. In particular, Fe_3O_4 and MnO exhibit lower voltage plateaus (around 0.6 V vs Li/Li^+[4,23]) during lithiation than the other TMOs, and thus appropriate for using as anode materials for LIBs. To date, most of the investigations are concentrated on individual oxides, such as Fe_3O_4 mesoporous microspheres,[24] carbon coated Fe_3O_4 nanospindles,[25] carbon–encapsulated Fe_2O_3 hollow nanoparticles,[26] mesoporous Fe_3O_4@C microcapsules,[27] Fe_2O_3/graphene and Fe_3O_4/graphene composite,[28,29] MnO nanorods,[30] mesoporous MnO/C networks,[31] carbon-coated Mn_3O_4 nanorods.[12] However, no research is related to the composite oxides of Fe_3O_4 and MnO (Fe–Mn–O).

The coexistence of heterogeneous oxides could behave as dispersants of each other, thus will weaken the growth tendency of the oxides during calcining. Similarly, during electrochemical reactions as anode materials, the heterogeneous metals reduced from the composite oxides during lithiation are not liable to aggregate, nor are the heterogeneous oxides formed during delithiation. Combining these factors with the merits of Fe_3O_4 and MnO, in this work, we prepared Fe–Mn–O oxides with various Fe/Mn molar ratios by a general coprecipitation method followed by coating carbon using pyrrole as the carbon source. The carbon-coated composite oxides exhibit superior cycling performance and rate capability compared with the individual Fe_3O_4 or MnO prepared under the same conditions.

Received: June 6, 2013
Accepted: September 5, 2013
Published: September 5, 2013

dx.doi.org/10.1021/am402205z | ACS Appl. Mater. Interfaces 2013, 5, 9470–9477

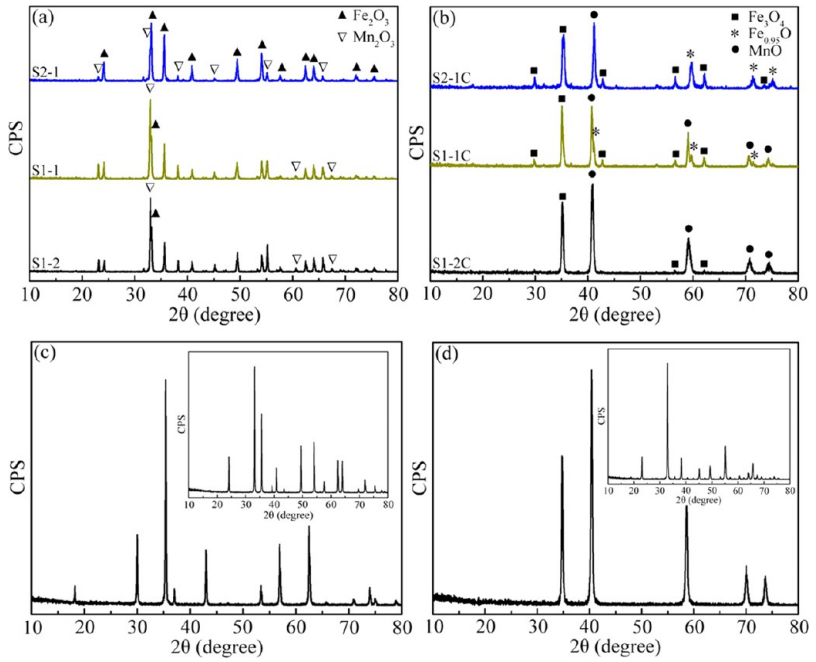

Figure 1. XRD patterns of (a) the as-sintered products S2−1, S1−1, and S1−2; (b) carbo-coated products S2−1C, S1−1C, and S1−2C; carbon-coated (c) Fe_3O_4 and (d) MnO. The insets in c and d are the corresponding XRD patterns of the as-sintered Fe_2O_3 and Mn_2O_3.

2. EXPERIMENTAL METHODS

2.1. Preparation of Carbon-Coated Fe−Mn−O. All the reagents are analytically pure and used without further purification. During the preparation of Fe−Mn−O composite oxides with a Fe/Mn molar ratio of 2:1 (designated as S2−1), 16.21 g of $FeCl_3{\cdot}6H_2O$, and 5.94 g of $MnCl_2{\cdot}4H_2O$ were dissolved in 150 mL of deionized water to form uniform mixed solution, then the solution of 10 g NaOH dissolving in 50 mL deionized water was titrated into the mixed solution under magnetic stirring at ambient temperature. The precipitates were thoroughly washed with deionized water to remove the NaCl yielded, and then calcined at 600 °C for 5 h in a muffle furnace and air atmosphere. The preparation of Fe−Mn−O composite oxides with the Fe/Mn molar ratios of 1:1, 1:2 and 4:1 is similar to that of S2−1 except for the varied amounts of $FeCl_3{\cdot}6H_2O$ and $MnCl_2{\cdot}4H_2O$ reacted with the corresponding NaOH solution, and the as-sintered products are assigned to S1−1, S1−2, and S4−1 consecutively.

To realize fast carbon coating, 30 mL autoclaves made of 316L stainless steel (without lining) were adopted because they could undergo reactions at high temperature and high pressure. In this work, 1.5 g of Fe−Mn−O oxides were put into an autoclave and 0.51 mL of pyrrole was uniformly dropped into the oxide powders by a needle tubing. The tightly sealed autoclaves were then heated at 550 °C for 5 h in a muffle furnace and air atmosphere, and the products are the carbon-coated Fe−Mn−O oxides, which are denoted as S2−1C, S1−1C, S1−2C, and S4−1C, respectively. For comparison, Fe_2O_3 and Mn_2O_3 sintered at 600 °C for 5h were also coated with carbon by the same process.

2.2. Characterization of the Products. A Rigaku Dmax-2500 diffractometer with Ni filtered Cu Kα radiation (V = 50 kV, I = 100 mA) was utilized to collect X-ray diffraction (XRD) patterns at a scanning rate of 4° min^{-1}. The morphology of the products was examined using a JEOL JEM-2100 high-resolution transmission electron microscopy (HRTEM). Thermogravimetric (TG) analysis was performed from ambient temperature to 800 °C in air at a heating rate of 10 °C min^{-1} using a SDT thermal-microbalance apparatus to evaluate the carbon content. The content of carbon and nitrogen in the carbon-coated products was determined by a Vario EL III elemental analyzer. X-ray photoelectron spectra (XPS) were analyzed on a KARTOS XSAM800 X-ray photoelectron spectrometer (Kratos Analytical Ltd., Manchester, U.K.) using Al Kα radiation ($h\nu$ = 1486.6 eV) as the excitation source (V = 12 kV, I = 10 mA). Nitrogen adsorption/desorption isotherms were acquired at −196 °C in a Quadrasorb SI sorption analyzer with the samples being outgassed at 300 °C for 3 h under a vacuum in the degas port. The Brunauer−Emmett−Teller (BET) model was used to calculate specific surface area.

2.3. Electrochemical Test. The electrochemical performance of the Fe−Mn−O samples was tested using 2025 coin-type cells. The working electrodes are composed of 80 wt % Fe−Mn−O powders, 10 wt % acetylene black as conducting agent, and 10 wt % poly (vinylidene fluoride) as binder. The uniform slurry after mechanically stirring was coated on thin Cu foils, and dried in vacuum for 12 h at 120 °C. Metal Li foils were used as counter electrode, Celgard 2300 as separator, and a mixture of 1 M $LiPF_6$ solved in ethylene carbonate and dimethyl carbonate (1:1 by volume) as electrolyte. The weight of active material loaded on each disk (14 mm in diameter, punched from the Cu foils) is 3.0 mg or so. The assembly of the half-cells was carried out in an argon-filled glovebox at ambient temperature. The cells were discharged and charged at varied current densities in the voltage range of 0.02 and 3.00 V vs Li/Li^+ on a Land CT2001A battery test system at room temperature.

Cyclic voltammogram (CV) was measured on a PARSTAT 2273 electrochemistry workstation over the potential range of 0.01−3 V vs Li/Li^+ at a scanning rate of 0.3 mV s^{-1}, and electrochemical impedance spectra (EIS) were tested with an ac signal amplitude of 5 mV in the frequency range from 100 kHz to 0.1 Hz.

3. RESULTS AND DISCUSSION

3.1. XRD Results. The XRD patterns of the products sintered at 600 °C are shown in Figure 1a. All the diffraction peaks can be indexed to those from Fe_2O_3 (JCPDS card No. 79−1714) and Mn_2O_3 (JCPDS card No. 71−0636), implying the formation of composite oxides. The dominant phase is Fe_2O_3 in S2−1, and Mn_2O_3 in S1−2 as a result of the decreased Fe/Mn molar ratio from 2:1 to 1:2. After coating carbon, Mn_2O_3 was reduced to MnO (JCPDS card No. 75−0625), and most of Fe_2O_3 was reduced to Fe_3O_4 (JCPDS card No. 89−0688), as displayed in Figure 1b. In the patterns of S2−1C and S1−1C, some weak diffractions from $Fe_{0.95}O$ (JCPDS card No.

79−1967) could also be detected owning to the reduction of Fe_2O_3 during carbonization at 550 °C. The crystallite sizes of MnO and Fe_3O_4 in each sample were calculated by using the Scherrer formula and summarized in Table S1 in the Supporting Information. It is obvious from Table S1 in the Supporting Information that the crystallite size of MnO is approximate to that of Fe_3O_4 in the identical sample, especially in S2−1C, S1−1C, and S1−2C, demonstrating the well-codispersion of the two oxides in the product. And thus the average crystallite size of the carbon-coated product could be determined by averaging the crystallite sizes of the two oxides. The average crystallite sizes are about 20.6 nm for S2−1C, 30.4 nm for S1−1C, and 27.5 nm for S1−2C (The calculation details are in the Supporting Information), namely, when the Fe/Mn molar ratio is 2:1, the average crystallite size is smaller than those with lower ratios of 1:1 and 1:2. As a comparison, the XRD patterns of the carbon-coated Fe_3O_4 and MnO prepared under the same conditions are given in Figure 1c, d, from which the average crystallite sizes are 51.9 nm for Fe_3O_4 and 31.4 nm for MnO, apparently bigger than those of the Fe−Mn−O oxides. Thus the coexistence of heterogeneous oxides is conductive to inhibiting grain growth to some degree because the oxides could behave as dispersants of each other, and the dispersion is more effective at a higher Fe/Mn ratio of 2:1. The smaller crystallites could shorten Li-ion diffusion path when the composite oxides are used as anode materials for LIBs,[1,32] and thus is favorable for improving the electrochemical performance.

3.2. Average Particle Size Estimated by Specific Surface Area. According to the literature,[33] the average particle size can be approximately calculated by the BET surface area via the following equation

$$D_{BET} = 6000/\rho S$$

where D_{BET} is the average particle size (nm), ρ, the powder density (g cm^{-3}), and S, the specific surface area (m^2 g^{-1}) measured via the BET method. So the particle size could be reflected by the corresponding specific surface area to some degree, and the larger specific surface area demonstrates the smaller particle size.

To estimate the particle size of the Fe−Mn−O oxides, nitrogen adsorption/desorption isotherms of S2−1C, S1−1C, and S1−2C were measured, as displayed in Figure 2. The type II character of the isotherms is indicative of the nonporous structure of the carbon-coated products. The specific surface areas calculated by using the BET model are 26 m^2 g^{-1} for S2−1C, 11 m^2 g^{-1} for S1−1C, and 7 m^2 g^{-1} for S1−2C, from which the average particle sizes calculated are about 43.4, 102.5, and 161.1 nm (Because of the similar density of 5.18 g cm^{-3} for Fe_3O_4 and 5.45 g cm^{-3} for MnO, an average density of 5.32 g cm^{-3} was adopted to estimate the average particle size of the composite oxides), suggesting that the particle size increases with decreasing the Fe/Mn molar ratio from 2:1 to 1:1 and 1:2. In other words, the higher Fe/Mn molar ratio in the three samples is favorable to suppress the aggregation of crystallites into large particles.

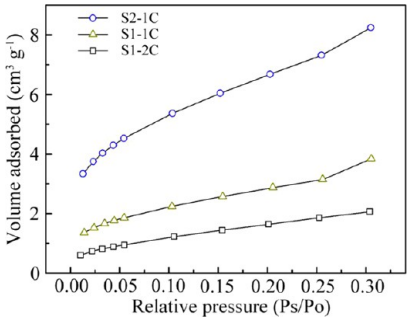

Figure 2. Nitrogen adsorption/desorption isotherms of S2−1C, S1−1C, and S1−2C.

3.3. TEM Observation. The carbon-coated Fe−Mn−O oxides were examined by HRTEM, as exhibited in Figure 3. From the images of S2−1C in images a and b in Figure 3, the particles are from several to tens of nanometers in diameter, and are coated with uniform thin carbon layers of about 5 nm in thickness. For S1−1C (Figure 3c, d), the particles ranging from 20 to 120 nm are coated with carbon coating of about 10 nm in thickness, and for S1−2C (Figure 3e, f), the particle sizes are from 20 to 200 nm with a carbon thickness of about 17 nm. Apparently, with decreasing the Fe/Mn ratio, the difference between the particle sizes in the identical sample increases, and more particles are over 100 nm in S1−2C. The thickness of the carbon coating becomes nonuniform in S1−2C. The TEM results are in good agreement with those from XRD and BET. From the TEM images of the carbon-coated Fe_3O_4 and MnO prepared under the same conditions as the carbon-coated Fe−Mn−O composite oxides (see Figure S3 in the Supporting Information), both the Fe_3O_4 and MnO crystallites agglomerate severely compared with the carbon-coated Fe−Mn−O composite oxides, though the carbon coating was formed uniformly on the particles. The particles of Fe_3O_4 range from 40 to 200 nm, and those of MnO from 50 to 150 nm, obviously bigger than those of the carbon-coated Fe−Mn−O oxides. The smaller particle size and the uniform thin carbon coating will be favorable for enhancing the electrochemical performance of the carbon-coated composite oxides.

3.4. TG and XPS Analysis. To evaluate the carbon content in the carbon-coated products, TG analysis was carried out, as shown in Figure 4a. The slight weight lose below 240 °C is attributed to the evaporation of water absorbed on the surface of the samples. The dominant weight loss between 350 and 550 °C is due to the oxidation of carbon, which is 11.1 wt % for S2−1C, 7.8 wt % for S1−1C, and 10.4 wt % for S1−2C. In addition, the elements of C, N were analyzed by an elemental analyzer. The weight percent of C and N are 11.14 and 1.89 wt % for S2−1C, 7.84 and 1.31 wt % for S1−1C, and 12.08 and 2.01 wt % for S1−2C, the C/N mass ratio close to 6:1 confirms the formation of N-doped carbon coating.

For further confirming the formation of N-doped carbon, the composition of the carbon-coated products was determined by XPS. Figure 4 displays the XPS of S2−1C. From the survey spectrum in Figure 4b, besides the elements of Mn, Fe and O, C and N are also the main elements in the sample. In Figure 4c, the peak located at 284.6 eV is related to the surface carbon,[34] while in Figure 4d, the peaks around 398 and 400 eV are resulted from pyridinic N (398.3 eV) and pyrrolic N (400.3 eV) in carbon materials, respectively.[35,36] The atomic ratio of 10:1 for C:N also verifies the formation of N-doped carbon coating. As has been reported,[37−39] the N-doped carbon coating could effectively improve the electrochemical performance because of the enhanced electronic conductivity.

3.5. Cycling Performance. The cycling performance of the carbon-coated products was tested at a current density of 100 mA g^{-1}, as shown in Figure 5a. S2−1C exhibits an initial discharge capacity of 1023.5 mAh g^{-1}, which is higher than

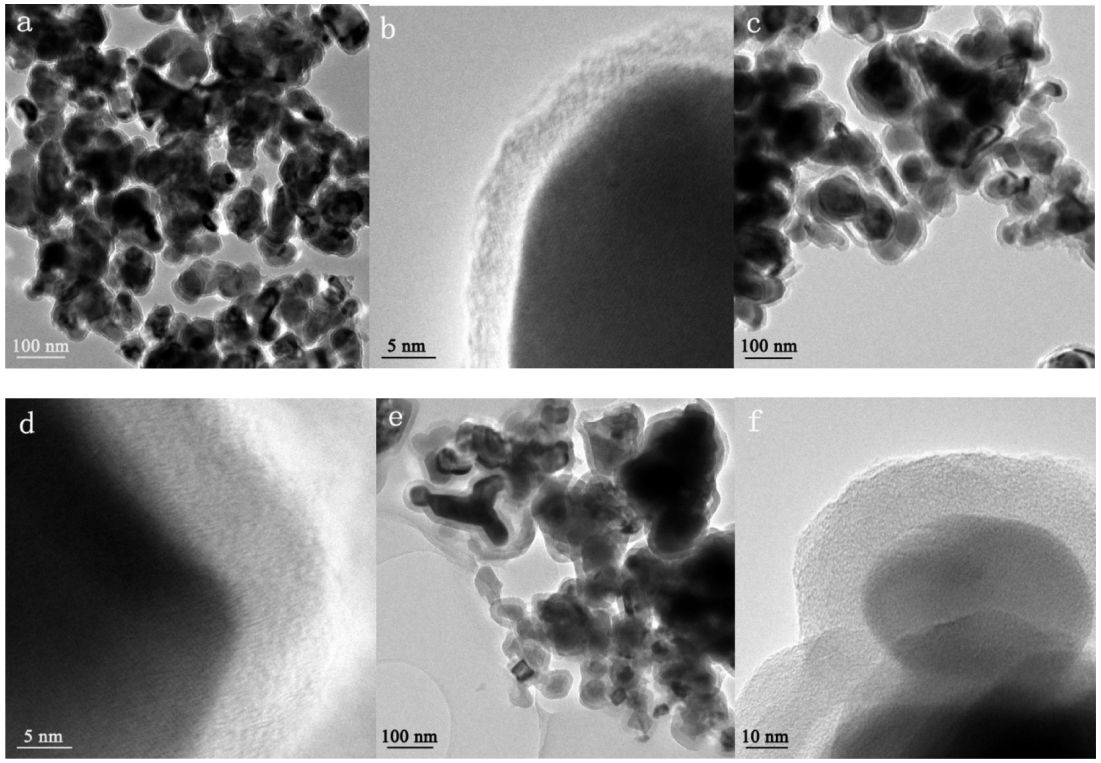

Figure 3. TEM images of (a, b) S2−1C, (c, d) S1−1C, and (e, f) S1−2C.

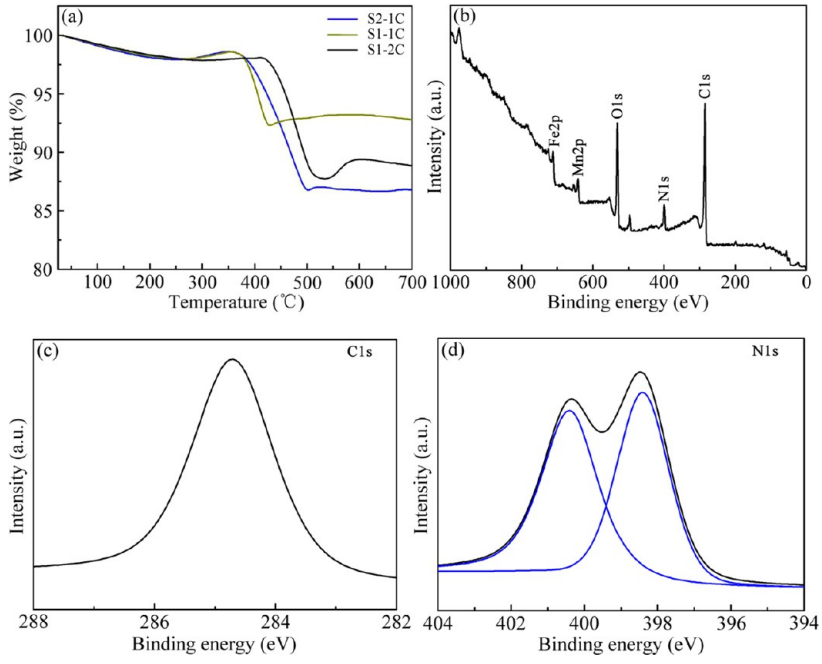

Figure 4. (a) TG curves of S2−1C, S1−1C, and S1−2C; and XPS spectra of S2−1C: (b) overall XPS, (c) C1s, and (d) N1s.

those of S1−1C (969.6 mA h g^{-1}) and S1−2C (864.9 mA h g^{-1}). Despite the low Coulombic efficiency of the first cycle due to the formation of solid electrolyte interface (SEI) films,[40−42] from the second cycle, the efficiency is more than 98%. After 90th cycle, S2−1C could deliver a discharge capacity of 651.8 mA h g^{-1}, much higher than those of S1−1C (553.6 mA h g^{-1}) and S1−2C (478.3 mA h g^{-1}). Though the discharge capacities of S1−1C and S1−2C are lower than that of S2−1C, they are yet superior to those of carbon-coated Fe_3O_4 and MnO (480.3 and 291.8 mA h g^{-1} after the 90th cycle, respectively) prepared under the same conditions (see Figure S4 in the Supporting Information), indicative of the advantages of the composite oxides over the individuals in cycling performance. The rise in capacity with the Fe/Mn molar ratio from 1:2 to 2:1 is to some extent related to the increased Fe content in the composite oxides, because Fe_3O_4 exhibits a higher theoretical capacity (926 mA h g^{-1}) than MnO (756 mA h g^{-1}). Furthermore, the better electrochemical performance of the carbon-coated Fe−

dx.doi.org/10.1021/am402205z | ACS Appl. Mater. Interfaces 2013, 5, 9470−9477

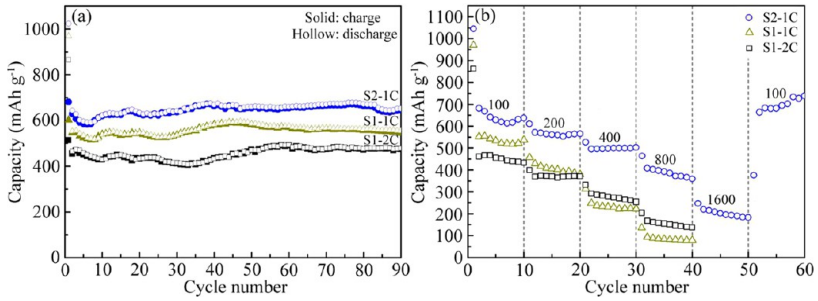

Figure 5. (a) Cycling performance at the current density of 100 mA g^{-1}, and (b) rate capabilities of S2−1C, S1−1C, and S1−2C.

Mn−O composite oxides than the individual Fe_3O_4 and MnO is also associated with the refinement effect resulted from the dispersion of the composite oxides. It is noted that the reversible capacities exhibit a slight rise with cycling, similar to what occurs in other oxides,[43−46] and the rise is ascribed to the activation of the oxides and to the formation of polymer/gel-like films due to the decomposition of the electrolyte. The activation gives rise to the decrease of electrochemical impedance, while the polymer/gel-like films are conductive to the mechanical cohesion and to the so-called pseudocapacitance-type behavior.[43−46]

From Figure 5a, it seems that the reversible capacity increases with the Fe/Mn molar ratio in the composite oxides, which is true for the samples with the Fe/Mn molar ratios of 2:1, 1:1 and 1:2. However, when the Fe/Mn molar ratio is increased to 4:1, the capacity decreases (433 mA h g^{-1} after the 20th cycle), as displayed in Figure S5 in the Supporting Information, because the dispersion effect of MnO and Fe_3O_4 weakens when the Fe/Mn molar ratio mismatches severely. The XRD pattern of S4−1C in Figure S2 and the average crystallite size in Table S1 in the Supporting Information further verifies the formation of large Fe_3O_4 crystallites, which should be responsible for the decreased capacity of S4−1C.

3.6. Rate Capability. The rate capability was evaluated at the current densities of 100, 200, 400, 800, and 1600 mA g^{-1} for every ten successive cycles, as revealed in Figure 5b. The reversible capacities of S2−1C are 637.3, 567.7, 501.3, 390.7, and 203.8 mA h g^{-1}, respectively. When the current density was restored to 100 mA g^{-1} after 50 cycles, the reversible capacity reaches 700.2 mA h g^{-1}, which is increased by about 9.8% compared to that in the initial ten cycles at 100 mA g^{-1}, further demonstrating the activation effect during cycling. The reversible capacities of S1−1C and S1−2C are listed in Table 1, which are obviously lower than those of S2−1C measured at the corresponding densities. The poorer rate performance of S1−1C and S1−2C is due to the larger crystallites and the agglomerated particles, because the smaller particles are favorable to shorten the diffusion path of Li ions.[1,32] From Figure 5b and Table 1, although S1−1C exhibits higher performance than S1−2C at the current densities below 200 mA g^{-1}, the rate performance of S1−2C at the current densities above 400 mA g^{-1} is better than that of S1−1C, partly due to the smaller crystallites in S1−2C than those in S1−1C and the better activation effect of S1−2C than S1−1C during cycling. Hence, it can be concluded that the smaller crystallites is beneficial to achieving high rate performance for these Fe−Mn−O oxides with different Fe/Mn molar ratios, which can well explain the superior cycling and rate performance of S2−1C to S1−1C and S1−2C.

Table 1. Reversible Capacities (mA h g^{-1}) of the Carbon-coated Products at Varied Current Densities (mA g^{-1})

	current density				
sample no.	100	200	400	800	1600
S2−1C	637.3	567.7	501.3	390.7	203.8
S1−1C	533.7	406.9	238.5	88.9	
S1−2C	450.7	373.5	279.6	156.2	

3.7. Electrochemical Impedance. For a better understanding the activation effect of the carbon-coated samples during cycling, the EIS of both the fresh and charged cells were measured, as shown in Figure 6. From Figure 6a, the Nyquist plot for the fresh cell of S2−1C contains a depressed semicircle in the high and medium frequency region followed by a linear tail in the low frequency region. The diameter of the semicircle is an indication of the charge-transfer resistance (R_{ct}) during the electrode reaction, and the inclined line represents the Warburg impedance (Z_w) associated with Li-ion diffusion kinetics.[47] The Nyquist plot for the charged cell of S2−1C exhibits the similar feature, however, the R_{ct} value (~20 Ω) is markedly lower than that of the fresh cell (~1300 Ω), indicating the greatly decreased contact and charge-transfer impedance, i.e., an obvious activation effect resulted from the cycling. The rapid electron transport accounts for the significant improvement in the cycling and rate performance. The activation is associated with the formation of SEI films which could not only enhance the mechanical cohesion but also give rise to the so-called pseudocapacitance-type behavior.[43−46] From Figure 6b, the Nyquist plot for the charged cell of S1−2C reveals a lower R_{ct} value (~100 Ω) at high frequency and a larger line slope at low frequency than S1−1C (~250 Ω), further demonstrating the better rate performance of S1−2C than S1−1C at high current densities above 400 mA g^{-1} (Figure 5b). Among the three carbon-coated samples, S2−1C possesses the lowest R_{ct} value and thus exhibits the most excellent performance.

3.8. Electrochemical Reaction. The electrochemical reactions during the charge/discharge of the carbon-coated samples were investigated by voltage/capacity plots and CV profiles. The charge/discharge plots for selected cycles are displayed in Figure 7a, c, and e. During the first discharging, S2−1C reveals two voltage plateaus at about 0.6 and 0.35 V, corresponding to the reduction of Fe_3O_4 to Fe[48] and MnO to Mn,[49] respectively. From the second discharging, a small voltage plateau at about 0.8 V implies the superposition of the reactions. During charging, the plateau presented around 1.75 V is due to the oxidation of Mn and Fe to MnO[31,50] and Fe_3O_4.[5,26] The concurrent reactions are reflected more clearly from the corresponding CV profile in Figure 7b, where the widened peaks with some weak fluctuations presented around

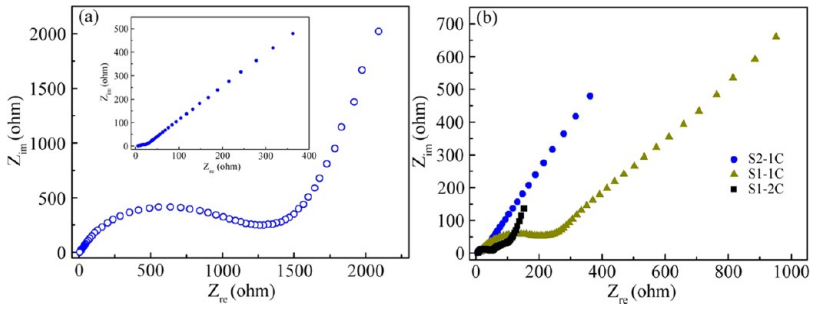

Figure 6. Nyquist plots of (a) the fresh and charged cells of S2−1C, and (b) the charged cells of S2−1C, S1−1C, and S1−2C. The inset in a is from the charged cell of S2−1C.

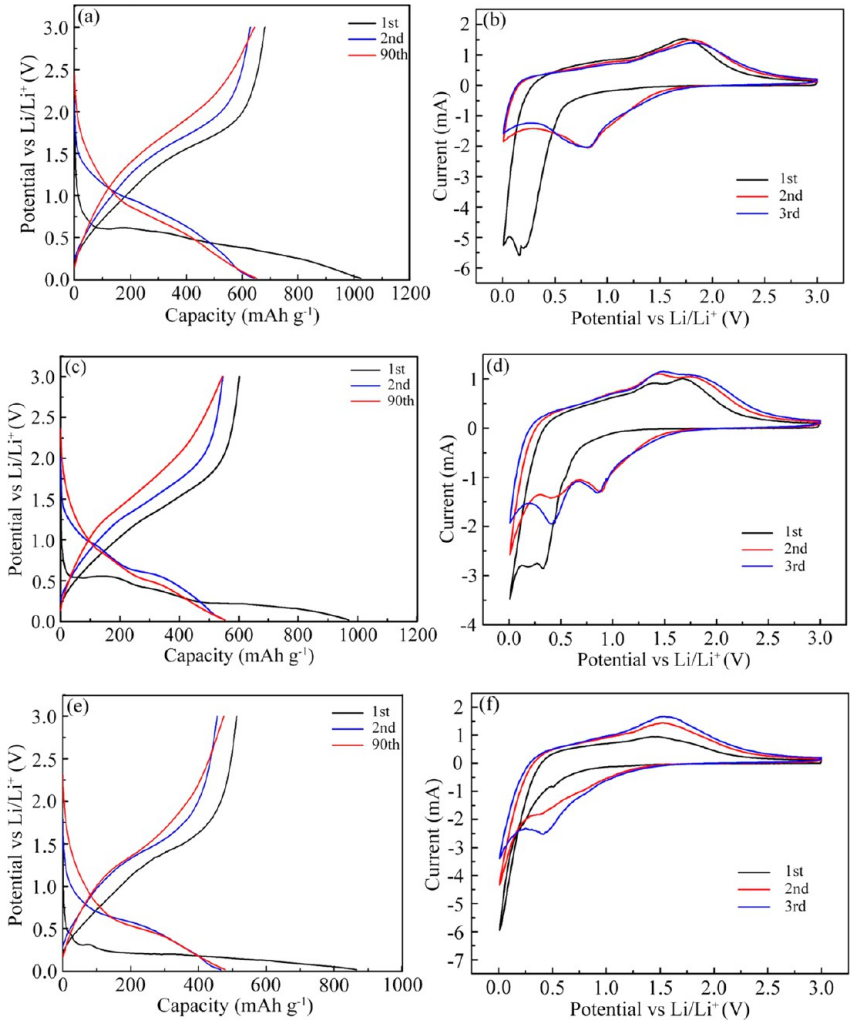

Figure 7. Discharge−charge plots for selected cycles at a current density of 100 mA g^{-1} and CV profiles at a scanning rate of 0.3 mV s^{-1} between 0.01 and 3.0 V vs Li/Li$^+$ of (a, b) S2−1C, (c, d) S1−1C, and (e, f) S1−2C.

1.75 V for the anodic process and 0.8 V for the cathodic process from the second cycle demonstrate the almost simultaneously occurred reactions. This further confirms the composite effect of the two oxides. From the second cycle, not only the charge profiles but also the discharge ones are analogous to each other, indicating the weak polarization in the S2−1C cells. Both the voltage/capacity plot and CV profile for the first cycle are different from those of the subsequent ones owing to the formation of SEI films during the first discharging.[40−42] For S1−1C, the first discharge profile exhibits two plateaus at about 0.55 and 0.35 V, and two distinguishable plateaus occur at 0.8 and 0.5 V in the subsequent cycles (Figure 7c). From the corresponding CV profile in Figure 7d, two cathodic peaks around 0.8 and 0.5 V and two anodic ones around 1.5 and 1.75 V from the second cycle clearly suggest that two reactions occur during both charging and discharging. For S1−2C, besides the main plateau around 0.3 V (MnO to Mn), a small one around 0.4 V (Fe_3O_4 to Fe) can also be distinguished in the first discharging plot (Figure 7e), because MnO is the dominant phase in the product. From the corresponding CV profile in Figure 7f, a clear cathodic peak around 0.5 V and a weak peak around 0.8 V can be observed, confirming that the main

dx.doi.org/10.1021/am402205z | ACS Appl. Mater. Interfaces 2013, 5, 9470−9477

reaction in this product associates with MnO. The difference in the curves of the three samples is resulted from the various Fe/Mn molar ratios in the products. Also from the CV plots, the second and third discharge profiles for both S1−1C and S1−2C do not overlap well, demonstrating that strong polarization occurred in these cells, which could further explain the better electrochemical performance of S2−1C than that of S1−1C and S1−2C.

As stated above, the electrochemical reactions in the carbon-coated samples could be described as follows:

$$Fe_3O_4 + MnO + 10e^- + 10Li^+ \leftrightarrow 3Fe + Mn + 5Li_2O$$

Combining the electrochemical measurement with the structure and morphology characterization, the following reasons might be responsible for the superior electrochemical performance of S2−1C. (1) The smaller crystallite size, thinner and more uniform carbon coating of S2−1C than S1−1C and S1−2C could shorten the diffusion path of Li-ions. (2) The coexistence of heterogeneous oxides (Fe_3O_4 and MnO) or elements (Fe and Mn) during the electrochemical reactions involved in the carbon shells could behave as dispersants of each other, alleviating the agglomeration of the congeneric substance. The mutual segregation of the heterogeneous substances is also one of the reasons why the electrochemical performance of the composite oxides is superior to that of individual Fe_3O_4 or MnO (Figure S4 in the Supporting Information). (3) The uniform N-doped carbon coating could ensure good electronic conductivity, buffer the large volume change, and prevent the nanoparticles from agglomeration, contributing to enhancing the electrochemical performance. As a consequence, the Fe−Mn−O composite oxides coated with the N-doped carbon exhibit better electrochemical performance than the individuals.

4. CONCLUSIONS

In summary, using pyrrole as the carbon source could form uniform N-doped carbon coating on Fe−Mn−O composite oxides. The carbon-coated oxides exhibit excellent electrochemical performance owing to the smaller particle size than the individual Fe_3O_4 or MnO, the mutual segregation of the heterogeneous oxides during charging and heterogeneous elements of Fe and Mn during discharging, as well as the enhanced electronic conductivity resulted from the N-doped carbon. The carbon-coated Fe−Mn−O composite oxides could be used as promising anode materials for high-performance LIBs.

■ ASSOCIATED CONTENT

Supporting Information

TEM images, XRD pattern of S4−1C, cycling performance of the carbon-coated Fe_3O_4, MnO, and S4−1C. This material is available free of charge via the Internet at http://pubs.acs.org.

■ AUTHOR INFORMATION

Corresponding Authors

*E-mail: byj97@126.com (Y.-J. Bai).

*E-mail: fan@sdu.edu.cn (R.-H. Fan). Tel/Fax: +8653188392315.

Notes

The authors declare no competing financial interest.

■ ACKNOWLEDGMENTS

This work was supported by the Independent Innovation Foundation of Shandong University, IIFSDU (2012ZD004), the Open Project from State Key Laboratory of Crystal Materials (KF1105), and the National Natural Science Foundation of China (50972076 and 51172131).

■ REFERENCES

(1) Poizot, P.; Laruelle, S.; Grugeon, S.; Dupont, L.; Tarascon, J. M. *Nature* **2000**, *407*, 496−499.
(2) Li, Y.; Zhu, C. L.; Lu, T.; Guo, Z. P.; Zhang, D.; Ma, J.; Zhu, S. M. *Carbon* **2013**, *52*, 565−573.
(3) Zhi, L. J.; Hu, Y. S.; El Hamaoui, B.; Wang, X.; Lieberwirth, I.; Kolb, U.; Maier, J.; Mullen, K. *Adv. Mater.* **2008**, *20*, 1727−1731.
(4) Zhong, K. F.; Xia, X.; Zhang, B.; Li, H.; Wang, Z. X.; Chen, L. Q. *J. Power Sources* **2010**, *195*, 3300−3308.
(5) Cui, Z. M.; Hang, L. Y.; Song, W. G.; Guo, Y. G. *Chem. Mater.* **2009**, *21*, 1162−1166.
(6) Chen, J.; Xu, L. N.; Li, W. Y.; Gou, X. L. *Adv. Mater.* **2005**, *17*, 582−586.
(7) Li, Y. G.; Tan, B.; Wu, Y. Y. *Nano Lett.* **2008**, *8*, 265−270.
(8) Stura, E.; Nicolini, C. *Anal. Chim. Acta* **2006**, *568*, 57−64.
(9) Lin, Y. M.; Abel, P. R.; Heller, A.; Mullins, C. B. *J. Phys. Chem. Lett.* **2011**, *2*, 2885−2891.
(10) Zhou, G. M.; Wang, D. W.; Li, F.; Zhang, L. L.; Li, N.; Wu, Z. S.; Wen, L.; Lu, G. Q.; Cheng, H. M. *Chem. Mater.* **2010**, *22*, 5306−5313.
(11) Zhang, M.; Qu, B. H.; Lei, D. N.; Chen, Y. J.; Yu, X. Z.; Chen, L. B.; Li, Q. H.; Wang, Y. G.; Wang, T. H. *J. Mater. Chem.* **2012**, *22*, 3868−3874.
(12) Wang, C. B.; Yin, L. W.; Xiang, D.; Qi, Y. X. *ACS Appl. Mater. Interfaces* **2012**, *4*, 1636−1642.
(13) Wang, Y. L.; Xu, J. J.; Wu, H.; Xu, M.; Peng, Z.; Zheng, G. F. *J. Mater. Chem.* **2012**, *22*, 21923−21927.
(14) Wang, G.; Wang, H.; Cai, S. B.; Bai, J. T.; Ren, Z. Y.; Bai, J. B. *J. Power Sources* **2013**, *239*, 37−44.
(15) Sathish, M.; Tomai, T.; Honma, I. *J. Power Sources* **2012**, *217*, 85−91.
(16) Li, J. F.; Xiong, S. L.; Li, X. W.; Qian, Y. T. *J. Mater. Chem.* **2012**, *22*, 23254−23259.
(17) Chen, Y.; Xia, H.; Lu, L.; Xue, J. M. *J. Mater. Chem.* **2012**, *22*, 5006−5012.
(18) Zhang, Q. M.; Shi, Z. C.; Deng, Y. F.; Zheng, J.; Liu, G. C.; Chen, G. H. *J. Power Sources* **2012**, *197*, 305−309.
(19) Zhong, J. Y.; Cao, C. B.; Liu, Y. Y.; Li, Y. N.; Khan, W. S. *Chem. Commun.* **2010**, *46*, 3869−3871.
(20) Cheng, H.; Lu, Z. G.; Ma, R. G.; Dong, Y. C.; Wang, H. E.; Xi, L. J.; Zheng, L. X.; Tsang, C. K.; Li, H.; Chung, C. Y.; Zapien, J. A.; Li, Y. Y. *J. Mater. Chem.* **2012**, *22*, 22692−22698.
(21) Pasero, D.; Reeves, N.; West, A. R. *J. Power Sources* **2005**, *141*, 156−158.
(22) Mai, Y. J.; Tu, J. P.; Xia, X. H.; Gu, C. D.; Wang, X. L. *J. Power Sources* **2011**, *196*, 6388−6393.
(23) Poizot, P.; Laruelle, S.; Grugeon, S.; Tarascon, J. -M. *J. Electrochem. Soc.* **2002**, *149*, A1212−A1217.
(24) Xu, J. S.; Zhu, Y. J. *ACS Appl. Mater. Interfaces* **2012**, *4*, 4752−4757.
(25) Zhang, W. M.; Wu, X. L.; Hu, J. S.; Guo, Y. G.; Wan, L. J. *Adv. Funct. Mater.* **2008**, *18*, 3941−3946.
(26) Zhou, J. S.; Song, H. H.; Chen, X. H.; Zhi, L. J.; Yang, S. B.; Huo, J. P.; Yang, W. T. *Chem. Mater.* **2009**, *21*, 2935−2940.
(27) Yuan, S. M.; Li, J. X.; Yang, L. T.; Su, L. W.; Zhou, Z. *ACS Appl. Mater. Interfaces* **2011**, *3*, 705−709.
(28) Zhang, M.; Qu, B. H.; Lei, D. N.; Chen, Y. J.; Yu, X. Z.; Chen, L. B.; Li, Q. H.; Wang, Y. G.; Wang, T. H. *J. Mater. Chem.* **2012**, *22*, 3868−3874.
(29) Su, J.; Cao, M. H.; Ren, L.; Hu, C. W. *J. Phys. Chem. C* **2011**, *115*, 14469−14477.

(30) Fang, X. P.; Lu, X.; Guo, X. W.; Mao, Y.; Hu, Y. S.; Wang, J. Z.; Wang, Z. X.; Wu, F.; Liu, H. K.; Chen, L. Q. *Electrochem. Commun.* **2010**, *12*, 1520−1523.
(31) Luo, W.; Hu, X. L.; Sun, Y. M.; Huang, Y. H. *ACS Appl. Mater. Interfaces* **2013**, *5*, 1997−2003.
(32) Aricò, A. S.; Bruce, P.; Scrosati, B.; Tarascon, J. M.; Van Schalkwijk, W. *Nat. Mater.* **2005**, *4*, 366−377.
(33) Baiju, K. V.; Shukla, S.; Sandhya, K. S.; James, J.; Warrier, K. G. K. *J. Phys. Chem. C* **2007**, *111*, 7612−7622.
(34) Wu, Y. P.; Fang, S. B.; Jiang, Y. Y. *Solid State Ionics* **1999**, *120*, 117−123.
(35) Jansen, R. J. J.; Bekkum, H. Van *Carbon* **1995**, *33*, 1021−1027.
(36) Wu, Z. S.; Ren, W. C.; Xu, L.; Li, F.; Cheng, H. M. *ACS Nano* **2011**, *5*, 5463−5471.
(37) Gong, C.; Bai, Y. J.; Qi, Y. X.; Lun, N.; Feng, J. *Electrochim. Acta* **2013**, *90*, 119−127.
(38) Gong, C.; Bai, Y. J.; Feng, J.; Tang, R.; Qi, Y. X.; Lun, N.; Fan, R. H. *ACS Appl. Mater. Interfaces* **2013**, *5*, 4209−4215.
(39) Lei, C.; Han, F.; Li, D.; Li, W. C.; Sun, Q.; Zhang, X. Q.; Lu, A. H. *Nanoscale* **2013**, *5*, 1168−1175.
(40) Shim, J.; Kostecki, R.; Richardson, T.; Song, X.; Striebel, K. A. *J. Power Sources* **2002**, *112*, 222−230.
(41) Zhao, Y.; Li, J. X.; Ding, Y. H.; Guan, L. H. *Chem. Commun.* **2011**, *47*, 7416−7418.
(42) Zhou, W.; Lin, L. J.; Wang, W. J.; Zhang, L. L.; Wu, Q. O.; Li, J. H.; Guo, L. *J. Phys. Chem. C* **2011**, *115*, 7126−7133.
(43) Cherian, C. T.; Sundaramurthy, J.; Kalaivani, M.; Ragupathy, P.; Kumar, P. S.; Thavasi, V.; Reddy, M. V.; Sow, C. H.; Mhaisalkar, S. G.; Ramakrishna, S.; Chowdari, B. V. R. *J. Mater. Chem.* **2012**, *22*, 12198−12204.
(44) Zhou, G. M.; Wang, D. W.; Li, F.; Zhang, L. L.; Li, N.; Wu, Z. S.; Wen, L.; Lu, G. Q.; Cheng, H. M. *Chem. Mater.* **2010**, *22*, 5306−5313.
(45) Han, F.; Li, W. C.; Li, M. R.; Lu, A. H. *J. Mater. Chem.* **2012**, *22*, 9645−9651.
(46) Wang, Z. Y.; Luan, D. Y.; Madhavi, S.; Hu, Y.; Lou, X. W. *Energ. Environ. Sci.* **2012**, *5*, 5252−5256.
(47) Wang, J. Z.; Zhong, C.; Wexler, D.; Idris, N. H.; Wang, Z. X.; Chen, L. Q.; Liu, H. K. *Chem.—Eur. J.* **2011**, *17*, 661−667.
(48) Wang, S. Q.; Zhang, J. Y.; Chen, C. H. *J. Power Sources* **2010**, *195*, 5379−5381.
(49) Liu, J.; Pan, Q. M. *Electrochem. Solid-State Lett.* **2010**, *13*, A139−A142.
(50) Zhong, K. F.; Zhang, B.; Luo, S. H.; Wen, W.; Li, H.; Huang, X. J.; Chen, L. Q. *J. Power Sources* **2011**, *196*, 6802−6808.